IJASS
International Journal of
Aeronautical and Space Sciences

ORIGINAL PAPER

A Comparative Study of Hypervelocity Impact Characteristics in Aluminum Whipple Shielding Through 3D Measurement and Numerical Analysis

Yurim Park[1] · YunHo Kim[2] · Changkyo Shin[1] · Chun-Gon Kim[1]

Abstract

Hypervelocity impact research is key to the designing of shielding systems to protect structures in low earth orbit with risk of space debris impact. Understanding the physical features contributes to the effective development of impact shielding design. In this study, the impact hole area, lip height, and debris cloud impact radius were investigated for impacts up to around 4 km/s for 6061-T6 aluminum panels of 3 mm thickness using a 2-stage light gas gun. Image analysis and 3D scanning were employed to measure the geometric features. Numerical analysis was conducted to simulate the experiment cases and the modeling was verified through comparison of the geometric features. The hole area and debris cloud impact radius showed gradually increasing trends with increasing impact velocity. The 3D scan measurements followed the image analysis, and considering the overall similarity between the 3D scan and numerical simulation, the numerical model satisfactorily reproduced and supported the experimental measurements.

Keywords Hypervelocity impact · Numerical analysis · Debris cloud · Whipple shield

1 Introduction

Various artificial satellites such as communication satellites and manned space structures like the International Space Station (ISS) are mostly located in the low earth orbit (LEO) and the number of micrometeoroid and orbital debris (MMOD) continue to rise to this day due to the long history of launches and recently accelerated commercial endeavors to space. MMOD impacts involves impact velocities that reach up to 72 km/s and such hypervelocity impacts on space structures can be catastrophic [1]. Collisions between satellites and debris have been reported and continue to be a risk to space structures [2, 3]. As such impacts can result in the termination of satellites and exponentially increase the number of debris, space agencies worldwide have proposed and

implemented systems to monitor such debris and take evasive maneuvers when in close proximity [4–6]. Thus, research on the material behavior under such high velocity and hypervelocity impacts is important in developing shielding systems and mechanisms [7, 8].

Methods to prevent and shield against catastrophic damage to space structures under hypervelocity impact are critical for their durability, integrity, and survivability [9–13]. Starting with the Whipple shield that has been applied to the ISS, numerous shielding mechanisms including the stuffed Whipple shield and multi-shock shields have been designed to minimize damage from possible hypervelocity impact and outer layer penetration [4, 14]. The impact phenomena of hypervelocity impact and the post-impact physical characteristics have been widely studied for various materials and structural configurations including thin metallic targets to honeycomb sandwich panels [15–19]. Greater understanding of the material behavior can be utilized to the development of more efficient shielding systems as the cost of launching payloads into space is immense and protecting such valuable assets throughout the mission lifespan of space structures is a key factor that is considered in space programs.

In this study, a 2-stage light gas gun was used to carry out hypervelocity impacts of up to around 4 km/s on

✉ Chun-Gon Kim
cgkim@kaist.ac.kr

[1] Department of Aerospace Engineering, KAIST, 291 Daehak-ro, Yuseong-gu, Daejeon 305-701, Republic of Korea

[2] School of Mechanical Engineering, Pusan National University, Busan 46241, Republic of Korea

homogeneous 6061-T6 aluminum panels of 3 mm thickness to investigate the effect of the impact velocity on the geometrical features of impact. In addition to visual inspection of the penetration hole and debris impact characteristics on the second bumper through hypervelocity impact experiments, numerical analysis was performed to simulate the hypervelocity impact of various projectile velocities. The experiment and numerical analysis were compared to verify the numerical analysis results. The comparisons were carried out to verify the reliability of the numerical analysis model, and the investigations of the post-hypervelocity impact formations and numerical analysis are expected to contribute to the accurate and effective development of impact shielding design and detection methods.

2 Methods and Materials

2.1 Specimen Preparation

Aluminum 6061-T6 plate specimens of 200×200 mm and thickness of 3 mm were prepared. The aluminum plates

Fig. 1 Experimental jig with aluminum plate specimens

were fixed to a jig so that all four sides of the plates were fixed as shown in Fig. 1. Two plates were fixed to a jig to from a Whipple shield configuration with a standoff distance of 87 mm. When fixed to the jig, the exposure area of the aluminum plates was 180×180 mm about the impact point or center of the plates. The jig was then fixed vertically to carry out impacts normal to the plates within the impact chamber of the hypervelocity impact setup detailed in the next section.

2.2 Hypervelocity Impact

For the hypervelocity impacts, a 2-stage light gas gun was used with 5.56 mm diameter aluminum 2017-T4 spheres as the projectile. Figures 2 and 3 show the schematic diagram and photograph of the 2-stage light gas gun used in this study. The mass of the spherical projectile was 0.25 g. Multiple diaphragms are used to seal two adjacent volumes of compressed air and the pressure in one is released rapidly to produce a significant pressure difference that ruptures the diaphragms through which the highly compressed air is released and accelerates a piston of high-density polyethylene (HDPE) to pressure uncompressed air or compressed hydrogen gas stored in the piston tube. This in turn then ruptures the third and last diaphragm and propels the projectile to the impact specimen. A magnetic and laser intervalometer setup was used to measure the projectile velocity and the impact specimens were fixed to a holding jig on all
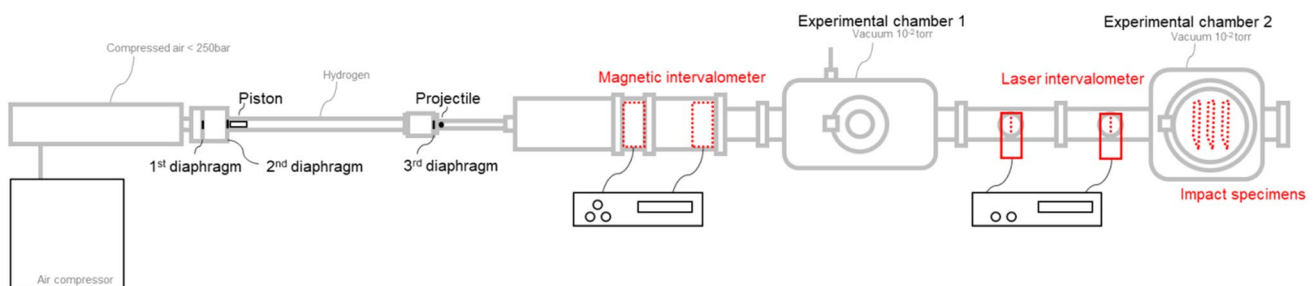

Fig. 3 The 2-stage light gas gun

Fig. 2 Schematic diagram of the 2-stage light gas gun

four sides to be normal to the projectile trajectory within the experimental chamber 2. High vacuum was established in the experimental chamber containing the impact specimen and the area of the specimen exposed for impact was 180×180 mm. Impact velocities were varied in the range of $0.44 - 4.06$ km/s to investigate the differences in the various post-impact characteristics, such as hard penetration and debris cloud formation, which are most distinct in relation to the impact velocity at the early portion of the hypervelocity range, based on the relative velocity distribution of orbital debris in LEO [20, 21]. The performance of dual wall systems like the Whipple shield for protection against MMOD is typically assessed using the ballistic limit equation (BLE) that defines the threshold particle size that causes perforation, and the BLE can be divided into 3 regions where region 1 generally covering impact velocities up to 3 km/s pertains to the deformation of the projectile and penetration through the first bumper, region 2 or the transitional velocity region generally covering 3–7 km/s pertains to the fragmentation of the projectile and the impact energy of the projectile is dispersed over a larger area in the form of a debris cloud to the second inner bumper, and region 3 beyond 7 km/s pertains to the complete fragmentation and melting of the projectile. Region 2 is typically a linear interpolation between the low and high points of region 1 and region 3; thus, this study incorporated impact velocities up to 4 km/s to investigate the impact phenomena characteristics of regions 1 and 2 since the impact features as a function of impact velocity can be considered consistent within region 2 [22].

2.3 Geometric Feature Measurements

The geometric features of the impacted specimens were measured. The measured features included the impact hole area of the impacted (front) side and the rear side of the specimens and the lip or rim height of the impact hole of both sides. The impact hole area was measured by analyzing the images of both sides of each specimen using software including Adobe Photoshop and ImageJ. While the impact hole can be measured by analyzing the images of the specimens, the lip height was too small for reliable measurement through such a method, so a 3D scanner was used to scan the impacted (front) and rear sides of each specimen for additional measurements. Space Spider of Artec3D was used to carry out the 3D scanning of the specimens, which produced. stl files for post-processing. A tripod was used to fix the 3D scanner at specified angles and the Artec Turntable was used to rotate the specimen at a constant rate as shown in Fig. 4. For post-processing of the 3D scans of the specimens, the browser-based mesh tool Meshy and the MPlane plugin of the CloudCompare software were used to measure the impact hole area and lip height.
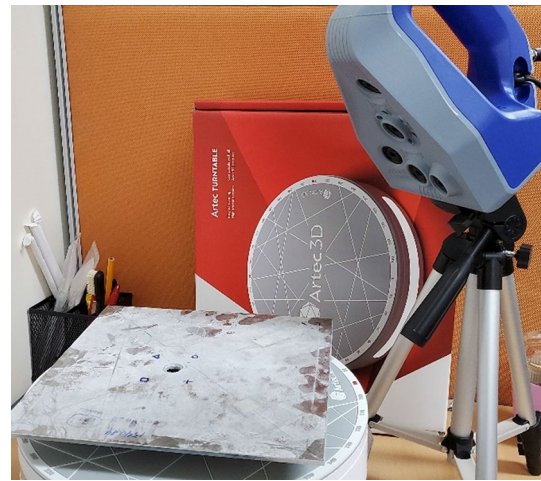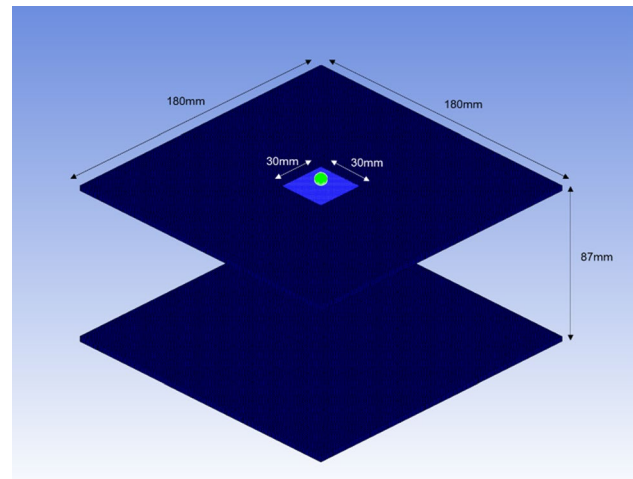

Fig. 4 The 3D scanning setup

Fig. 5 Numerical simulation modeling of the 2 bumper setup

2.4 Numerical Simulation

The experimental specimen setup and the impact cases were modeled and simulated through numerical analysis using the nonlinear dynamics analysis software Ansys Autodyn. The two bumper setup of the experiments was modeled with the same dimensions as the experiment as shown in Fig. 5. The aluminum sphere projectile was modeled with 5832 smoothed particle hydrodynamics (SPH) particles. Each aluminum plate was modeled with 97,200 hexahedral finite elements (FE) where 30×30 mm of the center of the first bumper was replaced with 190,333 SPH particles to adequately simulate the local impact characteristics at the center of the plate. A Lagrange–Lagrange FE/SPH coupling approach was used between the center SPH particles and the adjacent FE particles. For the SPH and FEM coupling, the node-to-mid-face-node "joins" function provided within
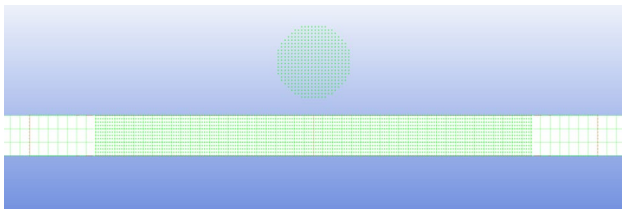
Fig. 6 The center region with the jointed FE and SPH particles

the software was utilized where SPH–Lagrange interaction was applied through the joining of the two domains, which is used to simulate a wide variety of phenomena including impact and penetration. For each FEM element, five SPH nodes were joined at the boundary of the 30×30 mm SPH region about the impact point or target center as shown in the cross section view of Fig. 6. The joined or fused nodes are regarding as single nodes in the calculations and will remain together until the join condition is removed through erosion. A Lagrangian mesh-free particle method, SPH is employed for the discretization of fluids or structures [23, 24]. SPH does not have the limitations in regards to large deformations that grid-based methods have as SPH discretizes the

domain with particles not topologically connected [25]. The coupling between the FE and SPH particles used the join module and the cross section of the adjoined region is shown in Fig. 6. Particle refinement or resolution can vary the outcome of the SPH simulation and this is commonly determined through the smoothing length, which is the spatial distance between the particles, so, literature that carried out a similar impact simulation using the smoothing length of 1/5 for accurate analysis was referenced [26]. Boundary conditions were applied to both bumper plates so that all 4 sides of each plate are fixed.

3 Experiment and Numerical Simulation Results

Hypervelocity impacts were carried out using the 2-stage light gas gun on aluminum Whipple shield configurations where the impact velocities ranged from 0.44 to 4.06 km/s. The thickness of the aluminum bumpers and the diameter of the spherical aluminum projectile were fixed. After the impact experiments were carried out, images of both sides of
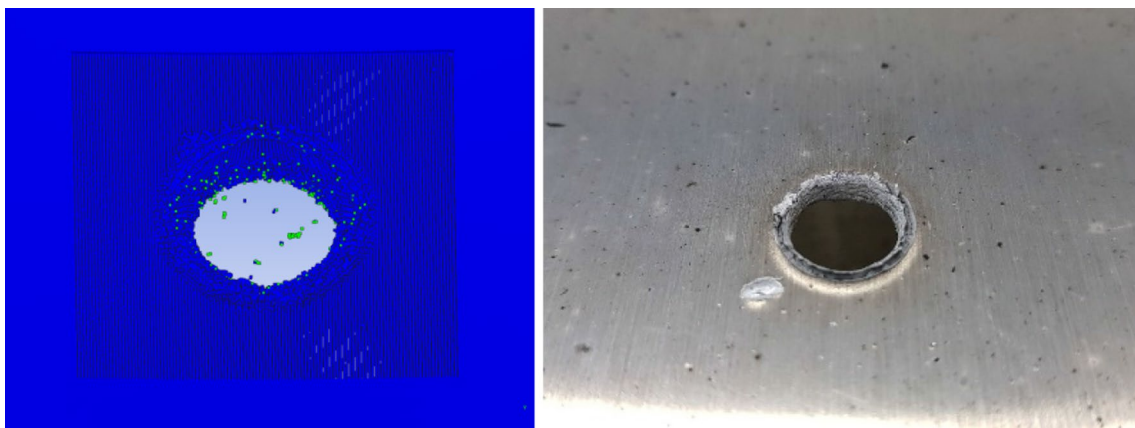

Fig. 7 Numerical simulation (left) and experiment case (right) for impact velocity 3.35 km/s
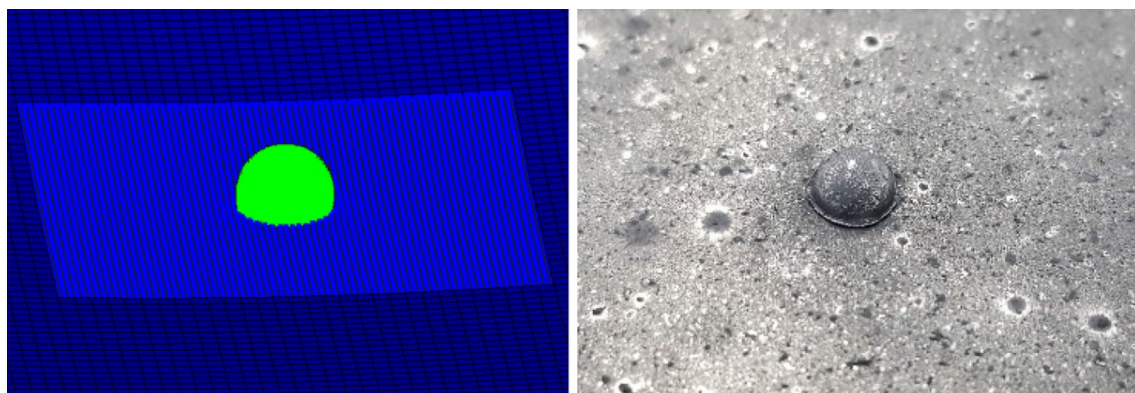

Fig. 8 Numerical simulation (left) and experiment case (right) for impact velocity 0.448 km/s

all the plate specimens were taken and 3D scans were taken for both sides of all the specimens for measurement of the various impact characteristics.

Numerical simulation was also performed to reproduce the experiment cases and compare the impact characteristic measurements to verify the reliability of the numerical analysis modeling for hypervelocity impact of aluminum Whipple shield configurations. The numerical simulations of each experiment case resulted in the same penetration or non-penetration phenomenon and geometrical features. As shown below in Figs. 7 and 8, the penetration case of impact velocity 3.35 km/s resulted in a similar lip or rim formation about the point of impact and the non-penetration case of impact velocity of 0.448 km/s resulted in the projectile failing to penetrate the plate and becoming partially embedded in the surface. Figures 7 and 8 both show the front side of a penetration case and non-penetration case, where the dark and light speckles visible on the target aluminum bumper surface are the broken off particles and burnt particles of the HDPE piston trailing behind the projectile after impact of the target bumper. The speckles in Fig. 8 are denser than Fig. 7 as the lower-impact velocity case utilized uncompressed air in the piston tube, resulting in greater burning compared to the higher-impact velocity case, which used compressed hydrogen gas. Also, as shown in Fig. 9, the debris cloud formation in the numerical simulation was observed and simulated properly through the SPH particle interaction between the projectile and the local impact region at the center of the plate specimen as well as the join coupling between the SPH particles of the local impact region and the FE of the remainder of the plate specimen.

3.1 Impact Hole Area

The area of the penetration hole after impact for the first bumper was investigated. For the experiment cases, the impact hole areas of the post-impact specimens were measured using image analysis as well as 3D scanning from both sides: the front (impacted) and rear sides. For each side, the 3D scan file was measured for the hole area using the Meshy software by selecting the desired cross section at the interior wall of the hole as shown in Fig. 10. The impact hole area was also measured from the numerical simulation results. The comparison of the impact hole area measurements is shown in the Fig. 11. It can be observed that the hole areas in relation to the impact velocity exhibit similar trends for the image analysis, 3D scan, and numerical simulation for both the front and rear sides. The hole areas measured from the 3D scan and the numerical simulation appear to be greater than the experiment image analysis results, which is in agreement with the experimental equation in literature for reference regarding the hole size in shields for aluminum projectiles and shields [27, 28]. Assuming
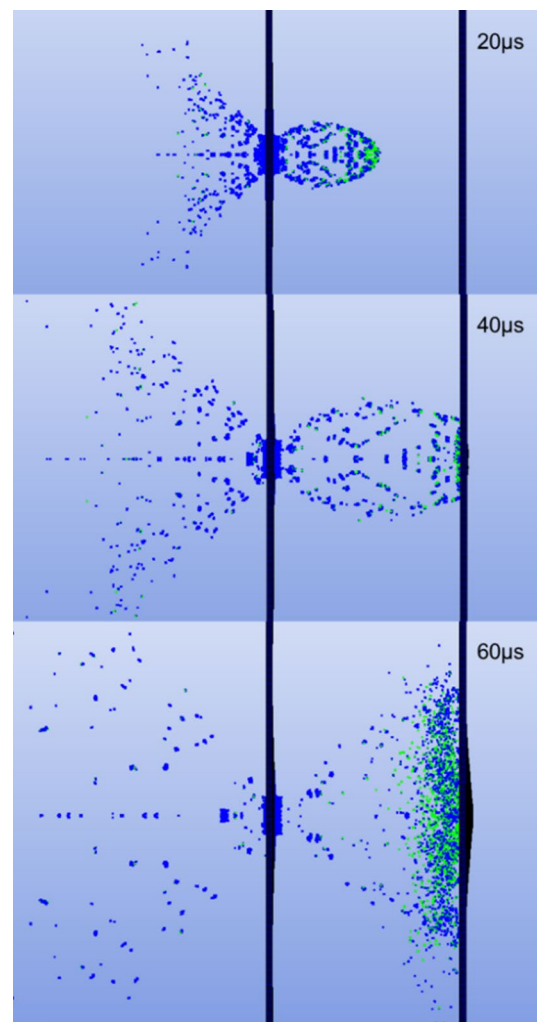

Fig. 9 Numerical simulation of debris cloud formation for the impact velocity of 4.06 km/s
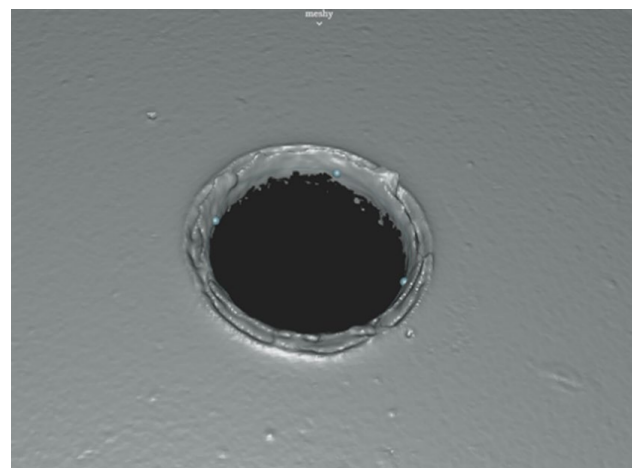

Fig. 10 Impact hole area measurement using Meshy for 3D scan files

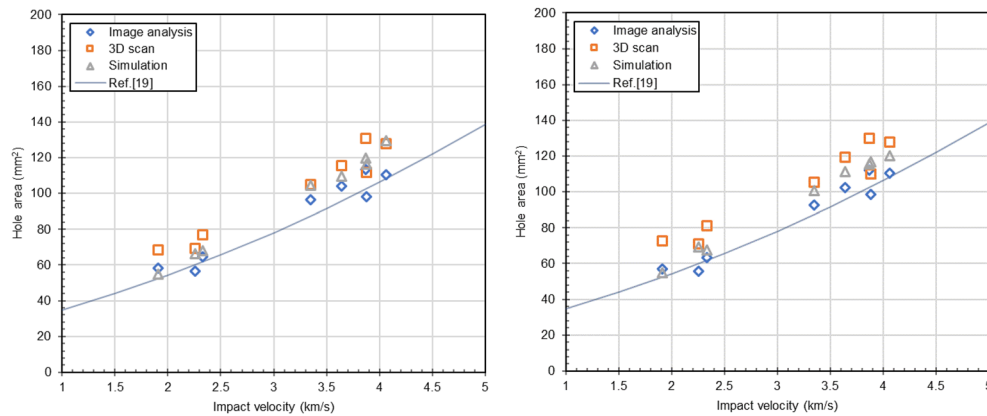that the literature employed a visual measurement method similar to the experiment image analysis of this study, the

Fig. 11 Impact hole area measurement comparison for the front side (left) and rear side (right)
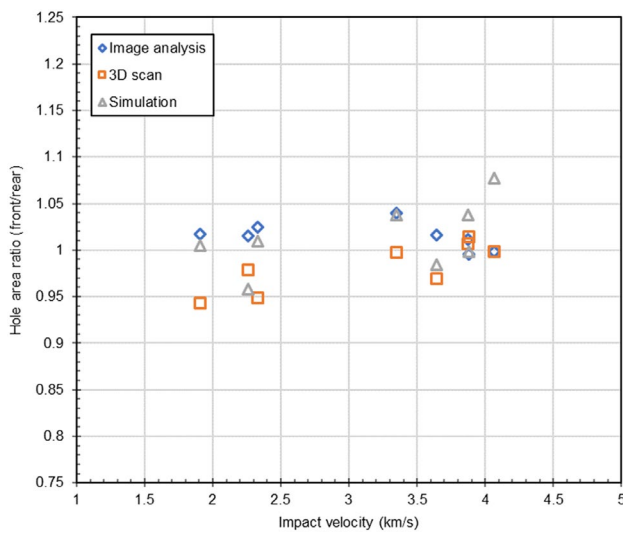

Fig. 12 Impact hole area ratio (front/rear) comparison

comparison result suggests that the 3D scan measurement and numerical simulation offer more accurate hole area measurements. The measurement data were very similar to each other, showing the validity of the numerical analysis model used. The relationship between the front and rear side impact hole areas is plotted for the image analysis, 3D scan, and numerical simulation in Fig. 12. The hole area of the front side was divided by the hole area of the rear side. As can be observed, while the change in the hole area ratio with impact velocity was not significant, the image analysis data did not exhibit a distinct increasing or decreasing trend but the 3D scan and simulation results appeared to suggest a gradually increasing trend as the impact velocity increased. Shortly after impact, two shock waves propagate away from the interface between the projectile and the target plate, so that rarefaction waves are produced toward the center of the projectile, resulting in projectile and target plate material ejection in an outward angled rearward direction opposite

the direction of impact. As the impact velocity increases, the rearward ejection of material becomes decreasingly fanned outward while one of the shock waves reflects back from the rear side of the plate as a rarefaction wave, resulting in the increased acceleration of particles radially towards the rear side of the plate [28, 29]. This chain of events in a short period of time during impact may contribute in the greater increase in the impact hole area of the front side in relation to the rear side.

3.2 Impact Hole Lip Height

The lip or rim height of the impact hole was also measured for both sides of the aluminum plates. Image analysis was not possible for this measurement as the lip heights were in the mm-scale, so the lip height was measured using 3D scanning and from the numerical simulation. Fig. 13 shows the lip height measurement using 3D scanning and numerical simulation results. As can be observed in Fig. 14, the lip height measurement from the numerical simulation was greater than the measurement from the 3D scans. The 3D scan measurements for both the front and rear sides exhibited a gradually decreasing or virtually constant trend with increasing impact velocity while the numerical simulation measurement appeared to increase especially for the rear side lip height. The larger measurement of the numerical simulation and the increasing trend obtained are thought to be effects of the relatively low density of SPH particles employed in the projectile and local impact region, resulting in a greater sphere of influence for each particle contributing to the increased measurement values, as well as setting the SPH cutoff to limit the density of nodes to the cutoff density rather than deleting the node when the density of an SPH node drops below the minimum density or above the maximum density defined by the minimum and maximum density factor chosen for the material. For the impact lip height ratio, both the 3D scan and numerical
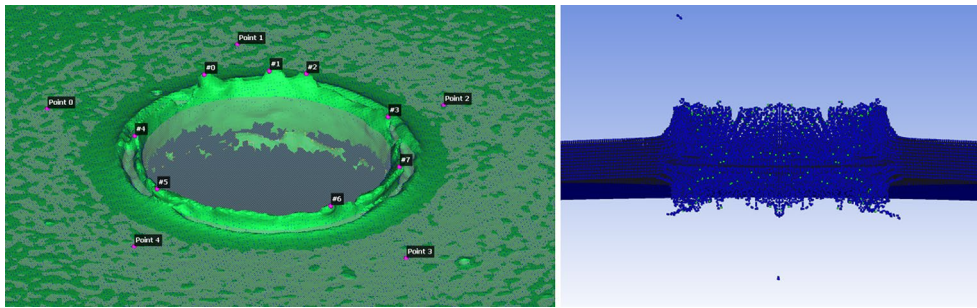
Fig. 13 Lip height measurement from the 3D scan (left) and numerical simulation (right)
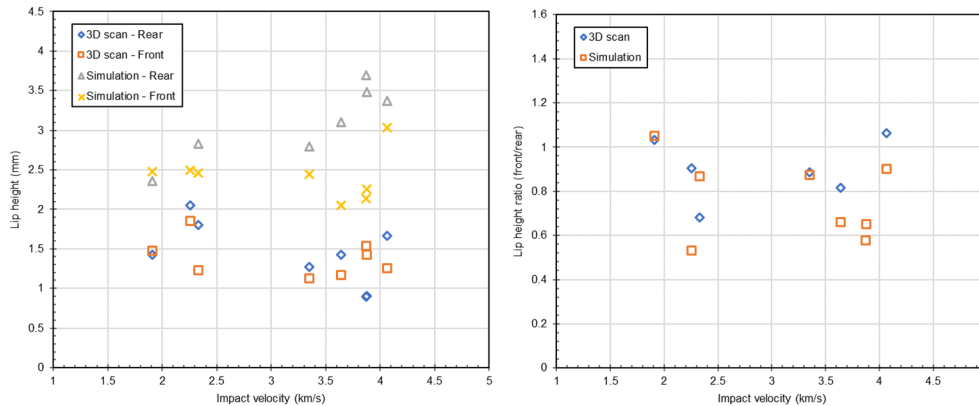

Fig. 14 Impact hole lip height comparison (left) and lip height ratio comparison (right)

simulation measurements had rear lip heights greater than the front side overall, and this can be explained by the angled rearward ejection of materials on the front side described in the previous section on impact hole areas, so the front side lip tends to be more angled outward than the rear side lip, hence resulting in the lip height ratio being less than 1. Considering the overall similarity between the 3D scan and numerical simulation measurements and the similar impact lip height ratio trend of not being affected by the impact velocity, the numerical simulation model satisfactorily reproduces and supports the experimental measurements.

3.3 Debris Impact Radius

After impact on the first bumper plate, the rarefaction waves produced in the target plate lead to fracture when the net tensile stress exceeds the fracture stress. Through this process, the projectile can be fragmented to significantly decrease the velocities of the fragments and this radial spreading of fragments, which also include the target plate material, is referred to as a debris cloud. This debris cloud impact on the second bumper was measured from the image analysis, 3D scan, and numerical simulation. The maximum radius of the debris cloud impact was measured. Only cases with debris cloud impact formations that have radial symmetry

from normal impact rather than oblique impacts were considered and other cases were excluded. The image analysis relied on visual inspection of the outermost point, the 3D scan relied on the outermost deformation point, and the numerical simulation looked at the yield stress contour plot of the impacted plate to measure the outermost debris impact point. Comparison of the impact debris maximum radius revealed that the image analysis, 3D scan, and numerical simulation all showed an increasing trend as the impact velocity increased as expected yet the image analysis measurement trend appeared to be far steeper than the 3D scan and numerical simulation results which were similar to each other. This result shows that there is a substantial amount of debris cloud material that is visually observable on the second bumper but did not produce a significant deformation on the second bumper surface. Similarly to the other measurements made in this study, the numerical simulation results were very similar to that of the 3D scan results as shown in (Figs. 15, 16).

4 Conclusion

In this study, the geometrical features of the impact hole area, lip height, and debris cloud impact radius were investigated for hypervelocity impacts of up to around 4 km/s on
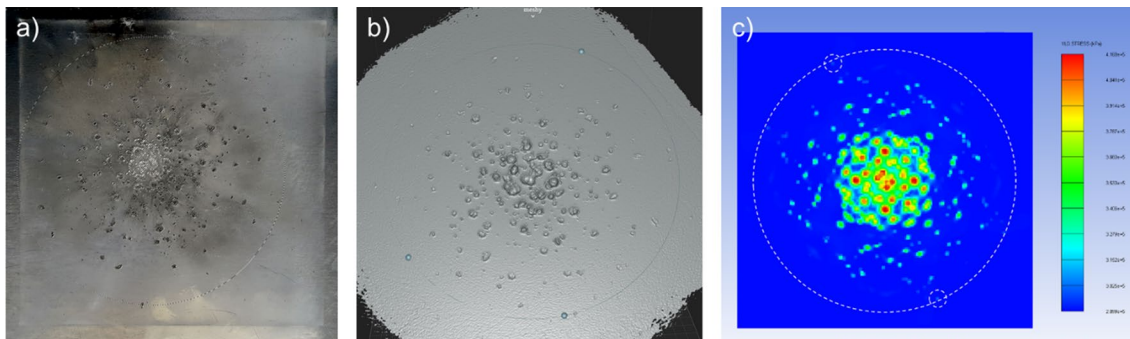
Fig. 15 Impact debris radius measurement method from the **a** 2D image processing, **b** 3D scan and **c** numerical simulation
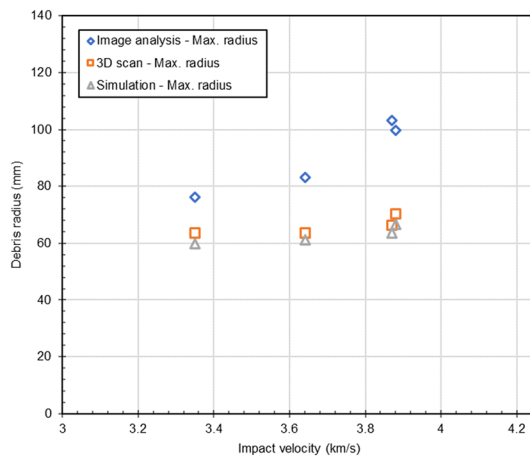

Fig. 16 Impact debris radius on the second bumper plate

homogeneous 6061-T6 aluminum panels of 3 mm thickness using a 2-stage light gas gun. In addition to image analysis, the geometrical features were measured using 3D scanning. Numerical analysis was carried out to reproduce the experiment results where the numerical simulation model incorporated the same dimensions of the experimentation. FE and SPH coupling was implemented to properly simulate the hypervelocity impact. For the impact hole area, the image analysis data did not exhibit a distinct increasing or decreasing trend but the 3D scan and simulation results appeared to suggest a gradually increasing trend as the impact velocity increased. The lip height measurement from the numerical simulation was greater than the measurement from the 3D scans. The 3D scan measurements for both the front and rear sides exhibited a gradually decreasing or virtually constant trend with increasing impact velocity while the numerical simulation measurement appeared to increase especially for the rear side lip height. Comparison of the impact debris maximum radius revealed that the image analysis, 3D scan, and numerical simulation all showed an increasing trend as the impact velocity increased as expected. The 3D scan measurements

followed the image analysis results and considering the overall similarity between the 3D scan and numerical simulation measurements, the numerical simulation model satisfactorily reproduced and supported the experimental measurements. For further study, the geometrical feature measurement comparison will be expanded to various plate thicknesses to investigate the influence of other parameters including the plate thickness.

References

1. Drolshagen G (2001) Hypervelocity impact effects on spacecraft. In: Warmbein B (ed) Proceedings of the Meteoroids 2001 Conference, 6–10 August 2001, Kiruna, Sweden. ESA SP-495, Noordwijk: ESA Publications Division, pp 533–541
2. Weeden B (2009) 2009 Iridium-Cosmos collision fact sheet. Secure World Foundation. Updated November 10, 2010
3. Limiting future collision risk to spacecraft: An assessment of NASA's meteoroid and orbital debris programs. Committee for the Assessment of NASA's Orbital Debris Programs, Aeronautics and Space Engineering Board, Division on Engineering and Physical Sciences, The National Academies Press, 2011
4. Christiansen EL (1993) Design and performance equations for advanced meteoroid and debris shields. Int J Impact Eng 14(1–4):145–156
5. Mehrholz D, Leushacke L, Flury W, Jehn R, Klinkrad H, Landgraf M (2002) Detecting, tracking and imaging space debris. ESA Bulletin 109
6. Africano JL, Stansbery EG, Kervin PW (2004) The optical orbital debris measurement program at NASA and AMOS. Adv Space Res 34(5):892–900
7. Cour-Palais BG (1987) Hypervelocity impact in metals, glass and composites. Int J Impact Eng 5(1–4):221–237
8. Clegg RA, White DM, Riedel W, Harwick W (2006) Hypervelocity impact damage prediction in composites: part I—material model and characterisation. Int J Impact Eng 33(1–12):190–200
9. Murr LE, Quinones SA, Ferreyra TE, Ayala A, Valerio OL, Hörz F, Bernhard RP (1998) The low velocity-to-hypervelocity penetration transition for impact craters in metal targets. Mater Sci Eng, A 256(1–2):166–182

10. See T, Albrooks M, Atkinson D, Simon C (1990) Meteoroid and debris impact features documented on the long duration exposure facility. DTIC Document

11. Baluch AH, Park Y, Kim CG (2013) Hypervelocity impact on carbon/epoxy composites in low Earth orbit environment. Compos Struct 96:554–560

12. Drolshagen G (2008) Impact effects from small size meteoroids and space debris. Adv Space Res 41(7):1123–1131

13. Christiansen EL, Hyde JL, Bernhard RP (2004) Space shuttle debris and meteoroid impacts. Adv Space Res 34(5):1097–1103

14. Cour-Palais BG, Crews JL (1990) A multi-shock concept for spacecraft shielding. Int J Impact Eng 10(1–4):135–146

15. Kang P, Youn S-K, Lim JH (2013) Modification of the critical projectile diameter of honeycomb sandwich panel considering the channeling effect in hypervelocity impact. Aerosp Sci Technol 29(1):412–425

16. Gehring Jr JW (1990) Chapter IV—Theory of impact on thin targets and shields and correlation with experiment, high-velocity impact phenomena. Elsevier, Academic Press, 1970//W.P. Schonberg, Hypervelocity Impact Penetration Phenomena in Aluminum Space Structures. J Aerosp Eng 3(3)

17. Rolsten RF, Wellnitz JN, Hunt HH (1964) An example of hole diameter in thin plates due to hypervelocity impact. J Appl Phys 35:556–559

18. Schonberg WP, Williamsen JE (1997) Empirical hole size and crack length models for dual-wall systems under hypervelocity projectile impact. Int J Impact Eng 20:711–722

19. Mespoulet J, Hereil P-L, Abdulhamid H, Deconinck P, Puillet C (2017) Experimental study of hypervelocity impacts on space shields above 8 km/s. In: The 14th Hypervelocity Impact Symposium 2017, Canterbury, Kent, UK, 24–28 April 2017

20. Ting W (2006) The consequences of using kinetic energy anti-satellite weapons. In: International network of engineers and scientists against proliferation, INESAP Information Bulletin No. 26, June 2006

21. Pardini C, Anselmo L (2000) SDIRAT: Introducing a new method for orbital debris collision risk assessment. In: International Symposium on Space Dynamics, Biarritz, France, 26–30 June 2000, pp 1–9

22. Schonberg WP (2016) Comment on the reimerdes ballistic limit equation for dual-wall structural systems. J Spacecr Rockets 53(3):584–586

23. Lucy LB (1977) A numerical approach to the testing of the fission hypothesis. Astron J 82:1013–1024

24. Gingold RA, Monaghan JJ (1977) Smoothed particle hydrodynamics: theory and application to non-spherical stars. Mon Not R Astron Soc 181(3):375–389

25. Pascal M, Heilig G, Lueck M, Sauer M (2015) Simulation and experiments of hypervelocity impact in containers with fluid and granular fillings. The 13th Hypervelocity Impact Symposium. Procedia Eng 103:365–372

26. Kim Y, Yoo J, Lee M (2012) Optimal design of spaced plates under hypervelocity impact. J Mech Sci Technol 26(5):1567–1575

27. Maiden CJ (1963) Investigation of fundamental mechanism of damage to thin targets by hypervelocity projectiles. GM Defense Research Laboratories

28. John WG (1970) Chapter IV—Theory of impact on thin targets and shields and correlation with experiment. In: Kinslow R (ed) High-velocity impact phenomena. Academic Press, pp 105–156

29. Jonathan MM (2013) Investigation of hypervelocity impact phenomena using real-time concurrent diagnostics. Dissertation, California Institute of Technology